Open-shell donor-pi-acceptor conjugated metal-free dyes for dye-sensitized solar cells

Journal:	*Molecular Systems Design & Engineering*
Manuscript ID	ME-ART-07-2020-000091.R1
Article Type:	Paper
Date Submitted by the Author:	11-Aug-2020
Complete List of Authors:	Sabuj, Md Abdus; Mississippi State University, Dave C. Swalm School of Chemical Engineering and Center for Advanced Vehicular Systems Rai, Neeraj; Mississippi State University, Dave C. Swalm School of Chemical Engineering

Journal Name

ARTICLE TYPE

Cite this: DOI: 00.0000/xxxxxxxxxx

Open-shell donor–π–acceptor conjugated metal-free dyes for dye-sensitized solar cells†

Md Abdus Sabuj and Neeraj Rai*

Received Date
Accepted Date

DOI: 00.0000/xxxxxxxxxx

Dye-sensitized solar cells (DSCs) have drawn a significant interest due to their low production cost, design flexibility, and the tunability of the sensitizer. However, the power conversion efficiency (PCE) of the metal-free organic dyes is limited due to the inability of the dye to absorb light in the near-infrared (NIR) region, leaving a large amount of energy unused. Herein, we have designed new DSC dyes with open-shell character, which significantly red-shifts the absorption spectra from their counterpart closed-shell structure. A small diradical character ($y < 0.10$) is found to be beneficial in red-shifting the absorption maxima into the NIR region and broadening up to 2500 nm. Also, the open-shell dyes significantly reduce the singlet–triplet energy gaps (ΔE_{ST}), increase the total amount of charge-transfer to the semiconductor surface, reduce the exciton binding energy, and significantly increase the excited-state lifetimes compared to the closed-shell systems. However, the closed-shell dyes have higher injection efficiency with increased intramolecular charge transfer (ICT) character. Our study reveals the design rule for open-shell DSC dyes to be able to absorb photons in the NIR region, which can increase the efficiency of the solar cell device.

Design, System, Application We utilize the open-shell character quantified using diradical index to tune the optical properties of a group of small organic molecules that are candidate chromophores for the dye-sensitized solar cells. We find that a small diradical index can be beneficial to push the absorption maximum into the near infrared region (NIR). This can significantly enhance the power conversion efficiency (PCE) of the dye-sensitized solar cells. Our work establishes a new approach to design solar cell materials for higher PCE as they utilize photons in the NIR region. This work provides synthesis targets for dye sensitizers to be used in organic dye based solar cells. As molecules show a relatively small diradical index (less than 0.2 at the B3LYP level of theory), these can also be synthetic targets for non-linear optical materials.

1 Introduction

The ever-increasing need for energy compels the scientific community to search for renewable energy sources. Dye-sensitized solar cells (DSCs) [1] are an attractive alternative energy source due to their excellent durability, low processing and fabrication cost, cleaner environmental footprint, exceptional performance under low-intensity light, and the ability to tune the photosensitizer to absorb light in a particular region of the solar spectrum [2,3]. The power conversion efficiency (PCE) of the DSC largely depends on the dye and its ability to absorb low energy photons in the near-infrared (NIR) region [4–6]. Designing a dye which absorbs light around 940 nm can increase the current of DSC device by 40 %. [5] Despite significant past effort in designing dye sensitizers, [7] the large energy gap between the frontier molecular orbitals (FMOs) of most available dyes prohibits the absorption of low-energy photons; thus, the majority of the photons are wasted as heat. Therefore, to-date, the PCE of the metal-free organic dyes has reached only 14% of the incident light, [8–12] leaving much room for improvement in the sensitizer design. Almost half of the total energy transferred through the sunlight is in the NIR region [13]; therefore, tailoring the dye molecular structure to absorb enough photons in the NIR region is of particular interest to increase the PCE of the DSCs. [11]

The metal-free organic dyes have high molar absorptivity, design flexibility compared to the ruthenium-based (Ru) dyes; whereas, the latter suffer from metal toxicity, reduced stability, and depleted ruthenium resources. [6,14,15] There are different approaches to design metal-free NIR dyes. The red-shift in the absorption wavelength is achieved by extension of the π-systems [16–23]. However, larger dyes are found to have a lower PCE due to the lower dye loading and unfavorable binding with the semiconductor surface; consequently, increasing the aggregation and recombination with the redox-shuttle [16,24,25]. Therefore, designing small dyes that can intensely absorb light in the NIR region is imperative to increase the solar cell PCE [4]. Another

* Dave C Swalm School of Chemical Engineering, and Center for Advanced Vehicular Systems, Mississippi State University, Mississippi State, Mississippi, USA 39762. Fax: +1 662 325 2482; Tel: +1 662 325 0790; E-mail: neerajrai@che.msstate.edu

† Electronic Supplementary Information (ESI) available: [Optimized ground-state geometric parameters, $NICS_{iso}(1)$ values, MO diagrams, and Cartesian coordinates are provided in the supporting information.]. See DOI: 00.0000/00000000.

efficient strategy for dye design is connecting an electron-rich donor (D) unit with electron-deficient acceptor (A) unit together by π-conjugation. This type of D−A arrangement can impart strong push-pull interactions in the π-conjugated system; therefore, the energy gap between the highest occupied molecular orbital (HOMO) and the lowest unoccupied MO (LUMO) is reduced either by the resonance structure D−A and $D^+ = A^-$, or by hybridization of the donor HOMO with acceptor LUMO [13]. However, the current dyes for DSC have a closed-shell electronic configurations with a highly aromatic backbone, a strong antiferromagnetic (AFM) coupling between the electrons in the FMOs, and large optical gap, inhibiting absorption in the NIR region.

Open-shell diradicals have potential applications in organic photovoltaic, nonlinear optics, charge storage devices, and in organic solar cells. [26–28] Diradicals with two unpaired electrons in the degenerate or nearly-degenerate non-bonding molecular orbitals have a reduced AFM coupling between the unpaired electrons; therefore, they have a unique electronic, optical, and magnetic properties. [26,29] A reduced AFM coupling compared to the closed-shell molecules facilitates delocalization of the unpaired electrons along the backbone. [28,30] This delocalized electronic topology of diradicals increases the π-conjugation along the molecular backbone and ensures higher thermodynamic stability. [28,30] The inherent low FMOs energy gap of open-shell diradicals compared to the closed-shell counterpart can potentially red-shift absorption spectra into the NIR region, [13,28,30–33] which is beneficial increasing the PCE of the DSC device. [4] Although, a significant amount of works have been performed on molecular based diradicals; [13,29,32,33] however, there is no evidence of open-shell diradical dyes particularly designed for DSC device.

Here, we have report open-shell diradical dyes for DSC device and correlate geometric, optical, and charge-transfer properties with the diradical character. In this regard, we have designed D−π−A open-shell diradical dyes (Fig. 1) by modifying the structure of the conventional dye, D35 with donor triphenylamine (TPA) and acceptor cyanoacetic acid (CAA) moieties, [34] and compared the geometric, optical, and charge-transport properties with the closed-shell counterpart. In particular, we replace the π-spacer with different substituents to tune electronic properties. [6,15,35–39] The ubiquitous D−π−A design framework induces efficient charge separation along the molecular backbone and reduces recombination process by ensuring large spatial separation between the donor group and semiconductor surface. [4,8] The thiophene π-spacer in the D35 dye is replaced with benzo[1,2-c;4,5-c′]bis[1,2,5]thiadiazole (BBT) and benzo[1,2-d:4,5-d′]bis([1,2,3]thiadiazole) (iso-BBT) [40] to tune quinoidal/open-shell and closed-shell character, respectively. BBT has a high electron affinity due to its non-classical structure with a hypervalent sulfur atom. [40,41] Therefore, BBT-based molecules have a high HOMO and lower LUMO energy levels than iso-BBT [40], which can reduce the HOMO–LUMO energy gap, facilitating admixing of the FMOs in the ground-state. [33] Also, the thiadiazole units of the BBT recovers aromatic stabilization energy in the open-shell ground-state, developing a diradical character. [41] Although BBT has been used as a π-spacer in DSC dyes, the diradical character (y) of these dyes has not been explored. [37,42,43]

To further tune the electronic properties of the designed dyes, thiophene is used at both the ends of BBT and iso-BBT [40]. This increases the effective π-conjugation and the planarity of the backbone, and broadens the absorption spectra of the dyes. [18,44–46] Also, our study on macromolecular systems show that the quinoidal thiophene recovers aromaticity in the open-shell ground-state, developing a polyradical character. [47] Moreover, N substitution on the dye increases the backbone planarity by reducing the H–H repulsions and fine tunes the HOMO energy level of the dyes with the redox-potential of the redox-shuttle, providing enough potentials for dye regeneration. Furthermore, to asses the effect of π-systems elongation, thieno[3,2-b]thiophene (thienothiophene) is used replacing the thiophene π-spacer, which increases the diradical character but reduce the dye regeneration energy. Our study indicates the open-shell dyes with diradical character $y < 0.10$ significantly red-shifted the absorption spectra in the NIR region. Therefore, designing dyes with small diradical character is a potential approach to consider to further increase the PCE of DSC device.

2 Methods

2.1 Theoretical background

The power conversion efficiency (η) [37] of a DSC device is calculated as follows:

$$\eta = \frac{FF \times V_{oc} \times J_{sc}}{P_{in}} \tag{1}$$

where, FF is the fill factor, which indicates the resistance during electron transfer, [4] V_{oc} is the open-circuit voltage, J_{sc} is the short-circuit current, and P_{in} is the incident solar power. The J_{sc} of the DSC is determined as [37,39]:

$$J_{sc} = \int_{\lambda} LHE(\lambda) \times \phi_{inject} \times \phi_{collect} d\lambda \tag{2}$$

where, LHE is the light harvesting efficiency, ϕ_{inject} is the electron injection efficiency, and $\phi_{collect}$ is the charge collection efficiency. $\phi_{collect}$ is constant for a particular DSC device, where the only variable is the different types of sensitizer used in the solar cell. Therefore, increasing the LHE and ϕ_{inject} efficiency increases J_{sc}. Also, J_{sc} is a function of the solar spectrum; therefore, designing dyes to absorb light in the NIR significantly increase the integration range, increasing J_{sc}. [6]. The LHE of a sensitizer is defined as [15,37]:

$$LHE = 1 - 10^{-f} \tag{3}$$

where, f is the oscillator strength corresponding to the maximum absorbtion (λ_{max}). A larger f value of a particular dye increase the LHE.

The electron injection efficiency (ϕ_{inject}) depends on the driving potential during electron injection (ΔG^{inject}) to the semiconductor conduction band, which is calculated as: [37]

$$\Delta G^{inject} = E^0 + E^* - E_{CB} \tag{4}$$

where, E^0 is the oxidation potential on the ground-state of the dye, E^* is the excitation energy corresponding the the maximum absorbtion spectra (λ_{max}), and E_{CB} is the conduction band energy of the semiconductor used. For the TiO_2 semiconductor, E_{CB} =

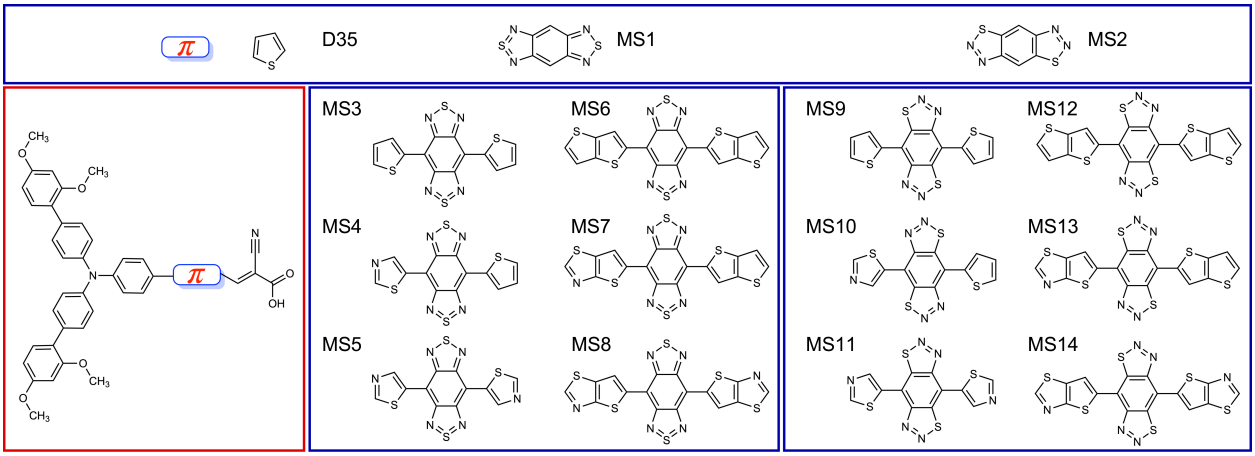

Fig. 1 Molecular structures of the parent (D35) and designed dyes (MS1–MS14).

4.0 eV. In calculating ΔG_{inject}, the ground-state oxidation potential (E^0) is approximated as negative of the HOMO energy of the dyes, according to Koopman's theorem.[37]

The open-circuit voltage (V_{oc}) of the dye is related with the energy level of the lowest unoccupied molecular orbital (E_{LUMO}) and E_{CB} as[48]:

$$V_{oc} = E_{LUMO} - E_{CB} \tag{5}$$

Therefore, an increased V_{oc} is realized by a higher energy level of LUMO of a particular dye. Also, the dye regeneration efficiency (ΔG^{reg}) calculated as[37]:

$$\Delta G^{reg} = E({I_3}^{-1}/I^{-1}) - E^0 \tag{6}$$

where, $E({I_3}^{-1}/I^{-1})$ is the oxidation potential for the redox-shuttle (-4.70 eV).[37] Therefore, a larger E^0 increases ΔG^{reg} of the sensitizer.

The percentage (%) of orbital contribution in excited-state transition of the open-shell dyes (MS3–MS8) is computed using the following equation[49]:

$$y(\%) = \frac{x_i^2}{\sum_{i=1}^{n} x_i^2} \times 100 \tag{7}$$

2.2 Computational details

All the calculations are performed with Gaussian 16 program package.[50] The geometry optimizations are carried out with the hybrid density functional, B3LYP[51,52] and 6-31G(*d, p*) basis set.[53] The residual force and density matrix converged with tight convergence criteria and ultrafine grid is used for the numerical integration. Frequency calculations are performed on each geometries to confirm local minima. Molecular geometries are fully relaxed without any symmetry constraints. Unless otherwise specified, analysis is performed with (U)B3LYP functional and 6-31G(*d, p*) basis set.

The open-shell character of the dyes characterized with the broken-symmetry (BS)[54] solution of the wave function. The diradical character (y) is calculated as an occupation number of the lowest unoccupied natural orbital (LUNO). The computed diradical character depends on the choice of density functional method (see Table S1).[55] Therefore, we have calculated diradical index with UBHandLYP and UCAM-B3LYP functionals, which incorporate different percentage of Hartree-Fock (HF) exchange. The diradical index calculated with UBHandLYP and UCAM-B3LYP on the UB3LYP geometry indicates a significant spin contamination in the ground-state for these small molecules (Table S2), leading to higher diradical index. However, the UB3LYP functional has low spin contamination than the two functionals considered. Also, B3LYP functional reproduced the bond lengths in small molecular systems.[32] Furthermore, studies on larger polymer indicate (U)B3LYP functional with 6-31G(*d, p*) basis set accurately predicts experimentally observed bandgap, albeit due to fortuitous cancellation of errors.[30] As we have correlated the diradical index with the HOMO energy level, which is directly related to the regeneration potential of the dye, UB3LYP functional is a reasonable choice in this case.

Aromaticity of the different functional moieties has been determined using nucleus independent chemical shift ($NICS_{iso}(1)$)[56] calculated with gauge-independent atomic orbital (GIAO) method[57,58] at 1 Å above the rings plane to account only for the π-electrons contribution on the aromaticity of the individual rings. A high negative ($NICS_{iso}(1)$) value indicates the corresponding ring as aromatic.

Time-dependent density functional theory (TDDFT)[59] calculations are performed on the ground-state geometries to obtain the excited-state properties. Benchmark calculations on the parent dye with different functionals are carried out as an increasing order of the percent (%) of Hartree-Fock (HF) exchange added to the functional, and compared the absorption maxima with the experimental data. The benchmark TDDFT calculations are performed with low HF exchange functionals, B3LYP (HF exchange = 20.0 %), APFD (HF exchange = 22.945 %)[60], and PBE1PBE (HF exchange = 25.0 %)[61]; functionals with intermediate HF exchange, BHandLYP (HF exchange = 50.0 %)[51], and M06-2X (HF exchange = 54.0 %)[62]; and long-range corrected functionals, CAM-B3LYP (HF exchange = 19.0 % short-range and 65% long-range)[63], and ωB97XD (HF exchange = 22.0 % short-range and 100% long-range)[64]. A single-point energy calculations performed to account only for the lowest 50 singlet excited-states.

Table 1 The computed singlet–triplet energy gap (ΔE_{ST}), energy of the FMOs, energy difference between the FMOs (E_g), and diradical index (y) of the parent (D35) and designed dyes (MS1–MS14), at (U)B3LYP/6-31G(d, p) level of theory and basis set. Energy values are provided in eV, and y is a dimensionless quantity.

Dye	ΔE_{ST}	HOMO	LUMO	E_g	y
D35	1.56	-4.87	-2.45	2.42	0.000
MS1	0.56	-4.96	-3.51	1.45	0.000
MS2	1.43	-5.02	-3.12	1.90	0.000
MS3	0.29	-4.76	-3.63	1.13	0.096
MS4	0.30	-4.85	-3.72	1.13	0.086
MS5	0.31	-4.90	-3.77	1.13	0.065
MS6	0.26	-4.74	-3.65	1.09	0.130
MS7	0.27	-4.81	-3.69	1.12	0.123
MS8	0.27	-4.84	-3.73	1.11	0.115
MS9	1.13	-4.84	-3.25	1.59	0.000
MS10	1.17	-4.91	-3.31	1.60	0.000
MS11	1.17	-4.94	-3.40	1.54	0.000
MS12	1.10	-4.82	-3.26	1.56	0.000
MS13	1.14	-4.90	-3.28	1.62	0.000
MS14	1.12	-4.91	-3.36	1.55	0.000

The TDDFT calculations are conducted in the presence of ethanol as an implicit solvent using the polarizable continuum model (PCM).[65,66]

3 Results and discussion

3.1 Ground-state geometric parameters of the parent and designed dyes

Bond lengths and dihedral angles are analysed to assess the degree of π-conjugation and planarity in the ground-state geometries (Fig. S1–S2). The D35 dye is twisted (θ_2 = 160°) at the single bond connecting the TPA donor and thiophene π-spacer, reducing the π-conjugation along the molecular backbone. The reduced π-conjugation in D35 is indicated by the large connecting bond between the TPA donor and thiophene π-spacer (a = 1.457 Å). The MS1 dye is more twisted than D35 (θ_2 = 150.6^0); however, the bond a in MS1 is smaller (1.455 Å) than D35, which is due to the efficient interlocking between the H of the TPA benzenoid ring and N of the BBT-spacer (H$\cdots$N) and a reduced steric repulsion due to the absence of H in the BBT-spacer. A large twist angle (θ_2 = 142°) is observed in case of the MS2 dye, which is the largest among all the dyes studied; therefore, reducing the π-conjugation along the MS2 dye backbone. The reduced π-conjugation is observed from a large connecting bond (a = 1.467 Å) of MS2 dye (Fig. S1), making it the least π-conjugated dye among all the dyes studied in this work.

The addition of thiophene and thienothiophene units to the dye backbone (see Fig. 1) significantly increases the planarity of the open-shell dyes when compared to the parent dye (D35).[18] The dihedral angle (θ_2) between the thiophene/thienothiophene and BBT π-spacer of the open-shell dyes (MS3–MS8) is close to 180° (Fig. S2), indicating a completely planar structure of the open-shell dye molecules. As a result, the bond a of the MS3–MS8 is reduced significantly (1.429–1.431 Å), indicating a more π-conjugated system in the open-shell dyes. The highly planar structure and increased π-conjugation of the open-shell dyes improves intramolecular charge transfer (ICT) along the dye backbone and red-shift the absorption spectra in the NIR region.[37,67] Also, N substitution in the thiophene and thienothiophene π-spacer further increases the dye planarity due to a reduced steric repulsion between the two H atoms of TPA donor and the adjacent thiophene and thienothiophene π-spacer. This type of planar geometries increase dye loading on the semiconductor surface as well.[67] However, the closed-shell dyes are less planar than the open-shell dyes.

The aromatic/quinoidal nature of a molecule is best identified by the bond length alternation (BLA), an increased BLA indicates a highly quinoidal backbone and a reduced BLA suggests an aromatic structure, respectively. Analyzing the bond lengths of the parent dye, D35 and designed dyes (MS1–MS14), it clear that bonds a, b, and c are smaller than a typical single bond (1.47 Å) but larger than a double bond (1.33–1.34 Å) (Fig. S1–S2). This indicates that, all the dyes have certain double bond character in the ground-state geometry, indicating the presence of π-conjugation in the dye backbone. The BLA of D35 is very small, indicating a complete aromatic structure of the dye. A reduced BLA is also observed for MS9–MS14 dyes as well (Fig. S1). This reduced BLA indicates that all these dyes have a closed-shell configuration in the singlet ground-state. The closed-shell structure of these dyes (D35, MS1–MS2, MS9–MS14) can be seen from the high negative NICS$_{iso}$(1) values along the backbone as well (Fig. S4). Even though, the bonds a and c in dye MS1 are comparable with the other closely related dyes (D35 and MS2), the length of bond b is close to a single bond, which significantly increases the BLA in the MS1 dye. This increased BLA indicates that the core of BBT unit in the MS1 dye has less aromatic character (reduced NICS$_{iso}$(1) of the BBT core, Fig. S4); therefore, MS1 is identified as a highly quinoidal closed-shell structure. The length of bond a in the MS3–MS8 dyes is reduced significantly due to the more planar structures of these dyes (Fig. S2), increasing the double bond character and BLA along the dye backbone. This further increase in the BLA increases the quinoidal character, which eventually develops diradical character in the ground-state for MS3–MS8 dyes.

3.2 Diradical character (y)

The contribution of the open-shell character to the ground-state can be quantitatively defined by the diradical index (y). The quantitative values of y define the degree of the open-shell character in the ground-state, such as, y = 0 indicates a closed-shell,

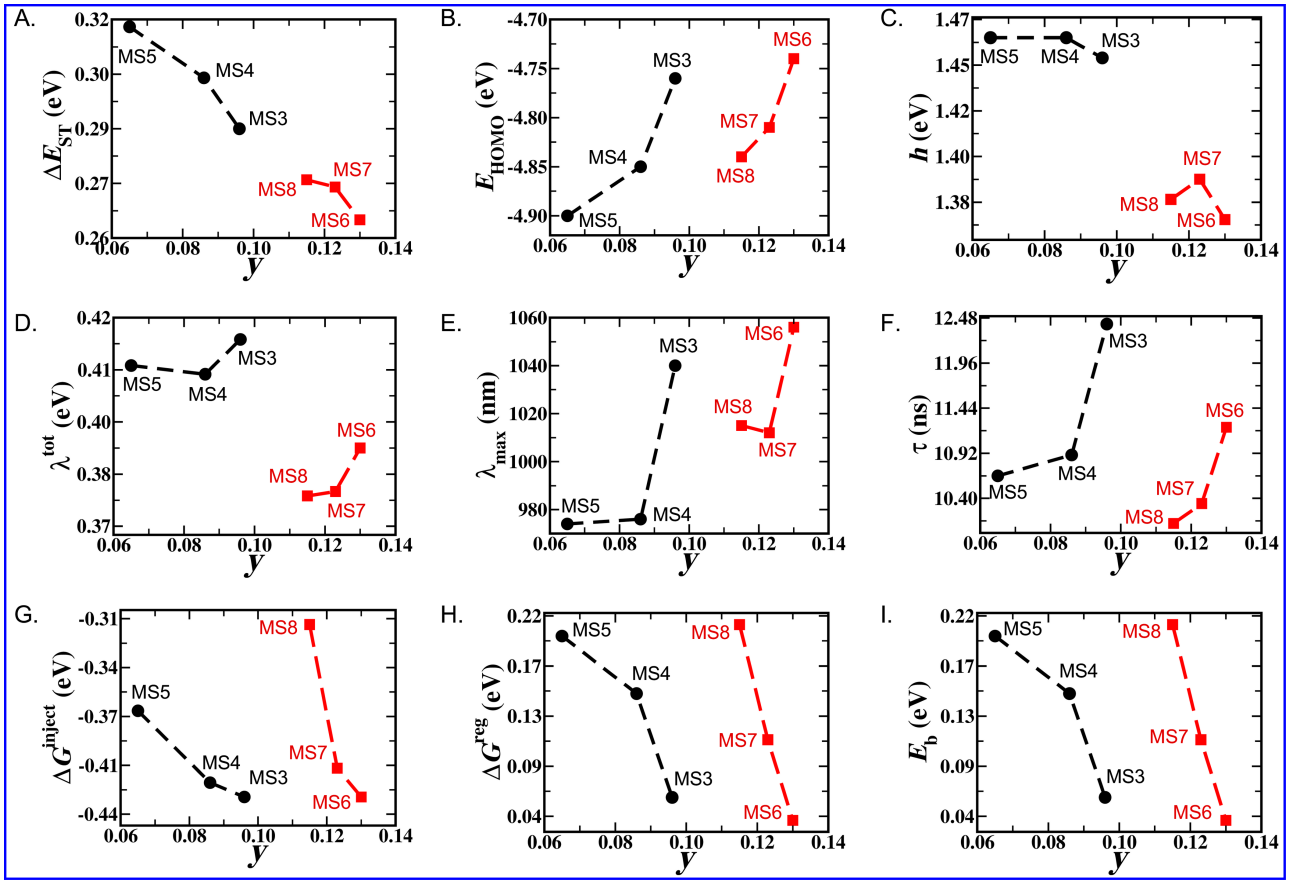

Fig. 2 The change in the electronic, optical, and charge-transport properties as a function of diradical character of the open-shell dyes, calculated at UB3LYP/6-31G(*d, p*) level of theory and basis set. (A) The predicted change in the singlet–triplet (ΔE_{ST}) energy gap, (B) energy level of the HOMO (E_{HOMO}), (C) chemical hardness (h), (D) the total reorganization energies (λ^{tot}), (E) wavelength (λ_{max}) of the maximum absorption peak, (F) excited-state lifetimes (τ), (G) potential for the charge injection (ΔG^{inject}) into the conduction band of TiO_2, (H) regeneration potential (ΔG^{reg}) of the dyes, and (I) exciton binding energy (E_b) with diradical index, y.

$0 < y < 1$ intermediate open-shell, and $y = 1$ is a pure open-shell configuration.[29,30] The calculated y values of the parent and designed dyes are provided in Table 1. Dye D35, MS1–MS2, and MS9–MS14 have a closed-shell structure ($y = 0$). However, dye MS3–MS8 develops diradical character, the maximum value is observed for dye MS6 ($y = 0.130$). The thiadiazole rings of the BBT π-spacer recovers aromaticity in the open-shell ground-state, as can be observed from the increased negative $NICS_{iso}(1)$ values compared to the closed-shell dyes (Fig. S4–S5). This increase in aromatic stabilization energy in the thiadiazole units of the BBT π-spacer facilitates C–C double bond breaking; therefore, developing diradical character in MS3–MS8 dyes. The calculated singlet–triplet (ΔE_{ST}) energy gaps of the closed-shell dyes are significantly higher than the open-shell dyes (Table 1) due to a high Coulomb repulsion in the closed-shell dyes. As the y values are increased, ΔE_{ST} is observed to decrease (Fig. 2A, S3) in the open-shell dyes.

MS3 dye has a very small y value and the diradical character decreased due to substitution of N in MS4 and MS5 dyes. Increasing the π-conjugation increases the y from MS3 ($y = 0.096$) to MS6 ($y = 0.130$). This increase in the y value is observed due to an increase in the quinoidal character in dye MS6 than MS3. An increased quinoidal character of MS6 dye can be observed from a less negative $NICS_{iso}(1)$ value of the BBT core in MS6 than MS3 dye (Fig. S5). A large y value increases the HOMO energy level of the dyes (Fig. 2B); therefore, reducing the energetic gap between the dye HOMO energy and oxidation potential of the redox-shuttle, which reduce the regeneration potential in the DSC device. The correlation between the calculated y value and HOMO energy level of the designed dyes (Fig. 2B) indicates that a small diradical index meet the design criteria of the sensitizer. Therefore, a small diradical index ($y < 0.10$) is helpful in designing organic dyes. At this range, a significant red-shift occurs in the absorption spectra, still providing enough regeneration potential to regenerate the dye. Given the sensitivity of the diradical index to the underlying density functional used in the calculation, our recommended range is applicable to methodology utilized in the current work. Furthermore, the open-shell dyes with small diradical character are a good candidate for non-liner optical (NLO), two-photon absorbtion (TPA), and ambipolar charge-transporting applications as well.[26,31,46,68,69]

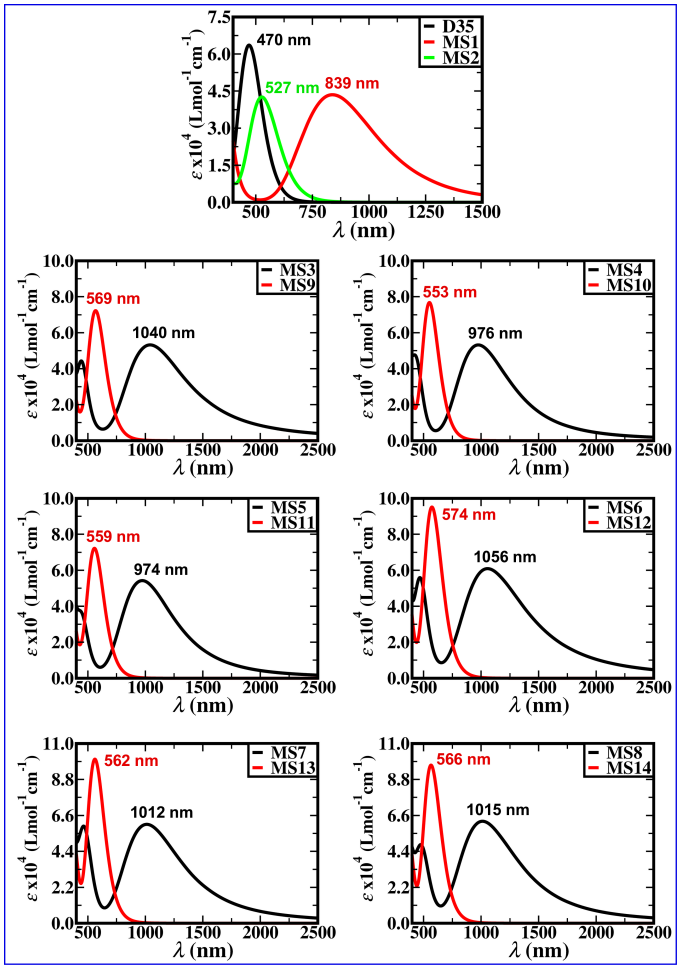

Fig. 3 The absorption spectra observed at PCM/TDDFT/(U)M06-2X/6-31(*d*, *p*) level of theory and basis set. Absorption spectra of the dyes plotted with their closed-shell and the corresponding open-shell structures.

3.3 Optical properties of the parent and designed dyes

The optical properties of the parent and designed dyes are calculated with time-dependent density functional theory (TDDFT). The benchmark calculations on the parent dye, D35 to select the appropriate functional is shown in Fig. S6. The absorption maxima predicted by the M06-2X functional (470 nm) is very close to the experimental value (463 nm) in ethanol.[70] Therefore, all the excited-state properties are calculated with M06-2X functional in ethanol solvent.

The absorption spectra of the parent and designed dyes are provided in Fig. 3. All the designed dyes (MS1–MS14) show significantly red-shifted absorption maxima than the parent dye, D35. However, the open-shell dyes have a more red-shifted absorption maxima than the closed-shell dyes. We would like to note that due to rotatable bonds through which these molecules can adopt different configurations (in solution), the λ_{max} does not exactly correspond to the vertical excitation energy of the lowest-energy geometry. The maximum absorption of MS1 and MS2 occurs at 839 nm and 527 nm, respectively, whereas, D35 absorbs only at 470 nm. This large change in the absorption wavelength indicates that the calculated spectra of MS1 and MS2 are red-shifted by 369 nm and 57 nm from the parent dye, respectively. It in interesting to note that the BBT π-spacer (MS1) significantly red-shifted the absorption maxima than the iso-BBT (MS2). This large shift in the absorption spectra of MS1 is due to the large quinoidal character, efficient π-conjugation, and more planar geometry of the MS1 dye than MS2 dye (Fig. S1, S4).[26,71]

Comparing the absorption maxima of open-shell dye MS3 and its closely related closed-shell dye MS9, the open-shell dye (MS3) red-shifts the maxima by 570 nm, whereas, the closed-shell dye (MS9) only red-shifts the maxima by 99 nm from the D35 dye. N substitution on the π-spacer increases the HOMO–LUMO energy gaps (Table 1); therefore, reducing the wavelength of the absorption maxima in open-shell dyes. Interestingly, the effect of N substitution on the absorption maxima is found to be greater in the open-shell dyes than the closed-shell dyes. A larger reduction in the absorption maxima is observed in case of the open-shell dyes than the closed-shell dyes. Elongation of the π-conjugation length in MS6 (open-shell dye) and MS12 (closed-shell dye) from MS3 (open-shell dye) and MS9 (closed-shell dye) red-shifts the absorption maxima by 16 nm and 5 nm, respectively. This indicates that increasing the dye conjugation length is more beneficial in case of the open-shell dye than the closed-shell dyes. Now, the absorption is red-shifted from the parent dye by 586 nm in MS6 and only 104 nm in MS12, respectively. Moreover, N substitution on the elongated dyes have similar effect as the small dyes, the absorption maxima shifts to lower wavelengths in the open-shell dyes than the closed-shell dyes.

The detailed spectral information of the closed-shell dyes are included in Table 2 and Table 3 contains excitation data for the open-shell dyes. In case of the closed-shell dyes, the most intense absorption occurs due to the excitation from the ground to the first excited-state ($S_0 \rightarrow S_1$), whereas, the maximum absorption occurs due to transitions from the ground to the second excited-states ($S_0 \rightarrow S_2$) in the open-shell dyes. The maximum absorption peak involved transferring electron from HOMO $\rightarrow$ LUMO, which indicates significant ICT character for all the designed dyes. Also, MO diagrams indicates that the HOMO is mainly localized on the TPA donor of the closed-shell dyes, with a small contribution on the thiophene π-spacer and CAA acceptor as well (Fig. S7). On the other hand, the LUMO has a major contribution on the CAA acceptor and most part of the thiophene π-spacer as well. As the size of the closed-shell dyes are increased (MS9–MS14), the HOMO–LUMO spatial separation is more visible; the HOMO is more localized in the TPA donor and LUMO is localized in the CAA acceptor and π-spacers. Further separation of the FMOs increases push-pull character in the dye molecular backbone, inducing more prominent ICT character. This localization of the LUMO in the CAA acceptor increases the overlap with the Ti 3d orbital; therefore, facilitating charge-transfer to the semiconductor surface.[72] In case of the open-shell dyes, the singly occupied MOs (SOMOs) have π-character and are delocalized over the whole backbone of the molecules (Fig. S8), which ensures the thermodynamic stability of these dyes.[28] The LUMOs of the open-shell dyes have major contributions in the π-spacers and CAA acceptor. This indicates a considerable admixing of the SOMOs and LUMOs of the open-shell dyes; therefore, reducing the ICT char-

Table 2 The optical properties for the closed-shell dyes at PCM/TDDFT/M06-2X/6-31(*d, p*) level of theory and basis set. The calculated excitations from the ground-state, energy associated with each states (E^*), the wavelength of the excitations (λ), oscillator strengths of the excitation (f), MOs involved in the transitions with percent contribution of the individual transitions. The reported transitions have oscillator strength, $f > 0.50$

Dye	States	E^*	λ	f	Orbital contributions	
D35	$S_0 \rightarrow S_1$	2.64	470.17	1.57	H→L (75.2%)	H-3→L (15.6%)
	$S_0 \rightarrow S_3$	4.04	306.88	1.16	H→L+2 (81.3%)	H-1→L (4.7%)
MS1	$S_0 \rightarrow S_1$	1.48	838.90	1.07	H→L (87.2%)	H-1→L (11.3%)
	$S_0 \rightarrow S_5$	3.37	367.48	0.54	H→L+1 (62.4%)	H-1→L+1 (28.5%)
	$S_0 \rightarrow S_{11}$	4.12	300.97	1.03	H→L+3 (75.2%)	H-1→L+3 (6.3%)
MS2	$S_0 \rightarrow S_1$	2.35	526.94	1.05	H→L (80.7%)	H-2→L (11.5%)
	$S_0 \rightarrow S_8$	4.10	302.64	0.54	H→L+2 (48.5%)	H→L+3 (8.5%)
	$S_0 \rightarrow S_9$	4.11	301.75	0.90	H→L+3 (72.8%)	H→L+2 (5.4%)
	$S_0 \rightarrow S_{50}$	5.97	207.67	0.51	H-5→L+3 (11.8%)	H→L+11 (11.7%)
MS9	$S_0 \rightarrow S_1$	2.18	568.60	1.78	H→L (62.0%)	H-1→L (27.9%)
	$S_0 \rightarrow S_4$	3.52	352.39	0.70	H→L+2 (45.4%)	H-1→L+2 (10.3%)
	$S_0 \rightarrow S_{10}$	4.02	308.45	1.11	H→L+5 (82.3%)	H-1→L+5 (4.7%)
MS10	$S_0 \rightarrow S_1$	2.24	552.90	1.88	H→L (60.0%)	H-1→L (25.9%)
	$S_0 \rightarrow S_4$	3.46	358.73	0.98	H→L+2 (56.4%)	H-1→L+2 (8.8%)
	$S_0 \rightarrow S_{10}$	4.07	304.93	0.85	H→L+5 (57.1%)	H-12→L (3.6%)
MS11	$S_0 \rightarrow S_1$	2.22	559.22	1.77	H→L (61.7%)	H-2→L (22.9%)
	$S_0 \rightarrow S_4$	3.45	359.73	0.96	H→L+2 (50.6%)	H-2→L+2 (9.6%)
	$S_0 \rightarrow S_{11}$	4.07	304.61	0.94	H→L+5 (75.2%)	H-1→L+9 (3.1%)
MS12	$S_0 \rightarrow S_1$	2.16	574.17	2.34	H→L (51.0%)	H-1→L (37.3%)
	$S_0 \rightarrow S_4$	3.41	363.16	0.87	H→L+2 (42.4%)	H-1→L+2 (11.2%)
	$S_0 \rightarrow S_{13}$	4.01	308.93	1.11	H→L+5 (79.4%)	H-1→L+5 (7.9%)
MS13	$S_0 \rightarrow S_1$	2.21	561.91	2.47	H→L (47.9%)	H-1→L (39.7%)
	$S_0 \rightarrow S_4$	3.33	372.63	0.99	H→L+2 (55.8%)	H→L (14.3%)
	$S_0 \rightarrow S_{14}$	4.07	304.88	1.13	H→L+5 (79.9%)	H-1→L+5 (6.3%)
MS14	$S_0 \rightarrow S_1$	2.19	566.03	2.38	H→L (46.4%)	H-1→L (35.7%)
	$S_0 \rightarrow S_4$	3.30	376.07	1.14	H→L+2 (51.6%)	H→L (10.4%)
	$S_0 \rightarrow S_{14}$	4.07	304.90	1.14	H→L+5 (80.3%)	H-1→L+5 (6.0%)

H = HOMO; L = LUMO

Table 3 Optical properties of the open-shell dyes at PCM/TDDFT/(U)M06-2X/6-31(*d, p*) level of theory and basis set. The calculated excitations from the ground-state, energy associated with each states (E^*), the wavelength of the excitations (λ), oscillator strengths of the excitation (f), MOs involved in the transitions with percent contribution of the individual transitions. The reported absorption transitions have oscillator strength, $f >$ 0.50. The percentage contribution of the orbitals to the excited-state is calculated with equation 7.

Dye	States	E^*	λ	f	Orbital contributions	
MS3	$S_0 \rightarrow S_2$	1.19	1040.10	1.31	H(α)→L(α) (63.2%)	H(β)→L(β) (19.8%)
	$S_0 \rightarrow S_7$	2.73	453.61	0.80	H(α)→L(α)+1 (26.7%)	H(β)→L(β)+1 (18.3%)
	$S_0 \rightarrow S_{34}$	4.03	307.80	1.00	H(α)→L(α)+4 (28.9%)	H(β)→L(β)+4 (36.2%)
MS4	$S_0 \rightarrow S_2$	1.27	976.09	1.31	H(α)→L(α) (56.0%)	H(β)→L(β) (22.0%)
	$S_0 \rightarrow S_8$	2.78	445.17	0.75	H(α)→L(α)+1 (21.7%)	H(β)-4→L(β) (16.2%)
	$S_0 \rightarrow S_{21}$	3.58	346.70	0.51	H(α)-13→L(α) (44.4%)	H(β)-13→L(β) (39.8%)
	$S_0 \rightarrow S_{35}$	4.06	305.13	1.03	H(α)→L(α)+4 (31.4%)	H(β)→L(β)+4 (37.7%)
MS5	$S_0 \rightarrow S_2$	1.27	974.41	1.33	H(α)→L(α) (55.1%)	H(β)→L(β) (22.7%)
	$S_0 \rightarrow S_8$	2.73	453.65	0.65	H(α)→L(α)+1 (24.1%)	H(β)→L(β)+1 (21.2%)
	$S_0 \rightarrow S_{20}$	3.57	347.51	0.55	H(α)-12→L(α) (49.5%)	H(β)-12→L(β) (38.9%)
	$S_0 \rightarrow S_{37}$	4.07	304.71	0.88	H(α)→L(α)+4 (28.7%)	H(β)→L(β)+4 (34.9%)
MS6	$S_0 \rightarrow S_2$	1.17	1055.68	1.49	H(α)→L(α) (19.5%)	H(β)→L(β) (59.5%)
	$S_0 \rightarrow S_7$	2.57	482.68	0.84	H(α)-4→L(α) (23.6%)	H(β)→L(β)+1 (20.0%)
	$S_0 \rightarrow S_{38}$	4.01	308.79	1.02	H(α)→L(α)+4 (27.9%)	H(β)→L(β)+4 (23.4%)
MS7	$S_0 \rightarrow S_2$	1.23	1012.43	1.48	H(α)→L(α) (22.5%)	H(β)→L(β) (56.0%)
	$S_0 \rightarrow S_6$	2.57	481.52	0.89	H(α)→L(α)+2 (24.1%)	H(β)→L(β)+1 (10.8%)
	$S_0 \rightarrow S_{39}$	4.06	305.48	0.67	H(α)→L(α)+4 (22.6%)	H(β)-12→L(β) (13.6%)
MS8	$S_0 \rightarrow S_2$	1.22	1014.67	1.53	H(α)→L(α) (56.9%)	H(β)→L(β) (21.7%)
	$S_0 \rightarrow S_6$	2.53	489.46	0.93	H(α)→L(α)+1 (23.4%)	H(β)→L(β)+1 (25.6%)
	$S_0 \rightarrow S_{42}$	4.07	304.45	0.90	H(α)→L(α)+5 (22.7%)	H(β)→L(β)+5 (28.0%)

H = HOMO; L = LUMO; α = spin-up; β = spin-down

acter. The spin density distribution (Fig. S8) also indicates the unpaired electrons are delocalized over the whole π-framework, increasing the stability of the open-shell dyes.[30]

The prominent ICT character of these dyes are clearly visible from the density difference plots, as shown in Fig. 4. The intramolecular charge-transfer is observed from the TPA donor to the CAA acceptor and part of the π-spacer adjacent to the acceptor. Also, the residual charges are localized in the CAA acceptor.

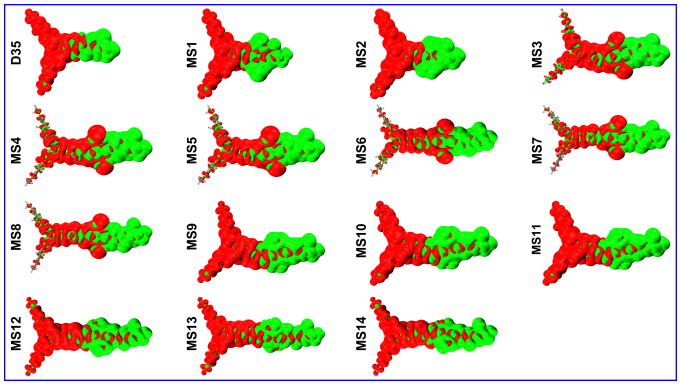

Fig. 4 The spin density difference ($\Delta\rho$) between the first singlet excited and ground electronic state ($\Delta\rho = S_1 - S_0$) at PCM/TDDFT/(U)M06-2X/6-31(d, p) level of theory and basis set
. The green and red surfaces represents the positive (electron enriched) and negative (electron depleted) regions shown at an isovalue = 0.00001 au, respectively.

Therefore, the designed dyes have enough available electrons to be injected into the semiconductor conduction band, facilitating charge-transfer to the semiconductor surface.[72].

The closed-shell dyes show absorption between 200–575 nm, whereas, the open-shell dyes absorb light in between 300–1056 nm range (Table 2, 3). Moreover, a small broadening of the absorption spectra is observed in the closed-shell dyes. However, in case of the open-shell dyes, the absorption spectra broadens to 2500 nm (Fig. 3), which increases the photocurrent of the DSC device.[44] Therefore, the closed-shell dyes absorption is limited to the half of the visible region of the solar spectrum, whereas, the open-shell dyes absorb light from the visible region to the whole NIR region. A broad spectra in the open-shell dyes (MS3–MS8) are obtained due to the delocalization of the MOs along the molecular backbone of the dyes (Fig. S8).[45]

3.4 Frontier molecular orbitals (FMOs) energy levels

The energy levels of the FMOs are provided in Fig. 5 with the energy gaps. All the designed dyes have HOMO energy levels well below the redox potential of the redox-shuttle, I_3^{-1}/I^{-1} (-4.70 eV)[37], which provides sufficient potential for regeneration.[15] Due to a large diradical character of the MS3 ($y \approx 0.10$) and MS6 ($y > 0.10$) dyes (Table 1), the HOMO energy levels are close to the redox potential, reducing the regeneration potential for these two dyes. The N substitution on the dye backbone lowers the HOMO energy levels, increasing the regeneration potentials. Also, most of the designed dyes have deeper HOMO energy levels than D35, which indicates regeneration efficiency of the designed is higher than the parent dye, D35. On the other hand, the LUMOs are observed at a sufficiently higher energy levels (> 0.20 eV)[42] than the TiO_2 conduction band, which indicates the capability of all the designed dyes to inject electron to the semiconductor surface. Also, the LUMO energy levels are significantly lowered in the BBT-based dyes than the iso-BBT-based dyes. A down-shift in the LUMO energy level reduce the HOMO–LUMO energy gaps (E_g), admixing the FMOs in the ground-state; therefore, developing diradical character in the MS3–MS8 dyes.[30,33]

All the designed dyes have significantly lower E_g values than the parent dye, D35 (2.45 eV), maximum reduction is associated in the open-shell dyes. It is also noteworthy that the quinoidal dye, MS1 also significantly reduce the E_g (1.45 eV) than the closed-shell dyes. Therefore, the observed E_g can be arranged in terms of electronic configuration as closed-shell > quinoidal > open-shell. In case of the parent and designed dyes, the order can be arranged as D35 > MS2 > MS13 > MS10 > MS9 > MS12 > MS14 > MS11 (closed-shell) > MS1 (quinoidal) > MS3 = MS4 = MS5 > MS7 > MS8 > MS6 (open-shell). This trend indicates that the open-shell dyes have most red-shifted absorption maxima, followed by the quinoidal and closed-shell dyes with reference to the parent dye (Fig. 3).

3.5 Ionization potential (IP) and electron affinity (EA)

The adiabatic IP and EA of the parent and designed dyes are provided in Table 4. The calculated IP of the open-shell dyes are smaller than the closed-shell dyes. The largest IP is obtained for the closed-shell dye MS2 (6.21 eV) and smallest IP is obtained for the open-shell dye MS6 (5.72 eV). A smaller IP indicates the open-shell dyes are more susceptible to loose electrons upon photoexcitation than the closed-shell dyes.[15,43,73] On the other hand, the EA of the open-shell dyes are higher than the closed-shell dyes, largest EA is obtained for the MS8 dye. This increased EA indicates the open-shell dyes can accept electron more easily than the closed-shell dyes with fast electron-transfer rate[28,43]; therefore, achieving increased PCE in the DCS.[74] Due to a reduced electron-electron coupling in the open-shell dyes, the electrons are loosely coupled with each other; thereby, decreasing the IP while increasing the EA in the open-shell dyes than the closed-shell dyes.[28] Furthermore, as the diradical character is increased, calculated IP and EA are observed to decrease in the open-shell dyes (Table 1 and 4).

The chemical hardness (h) is defined as a potential barrier to ICT in a dye, a smaller h is beneficial to charge-transfer. Therefore, the PCE of DSC is found to increase as h is decreased.[74] A reduced chemical hardness (h) is observed in the open-shell dyes than the closed-shell dyes (Table 4), which indicates the open-shell dyes should provide higher short-circuit current density, and a reduced charge injection efficiency; therefore, increasing the PCE of the DSC device.[15,74] Also, as the diradical index (y) of the open-shell dyes (MS3–MS5, and MS6–MS8) is increased, the h is observed to decrease (Fig. 2C), which indicates dyes with larger y should increase charge-transfer character. The chemical hardness (h) is obtained from the calculated values of IP and EA using the following equation:[15]

$$h = \frac{IP - EA}{2} \tag{8}$$

3.6 Reorganization energies (λ)

The charge-transfer rate is controlled by the reorganization energy of a dye (Marcus theory).[75] A smaller reorganization energy increases the charge-transfer (hole and electron) process.[76] As the inner (intramolecular) reorganization energy origins due

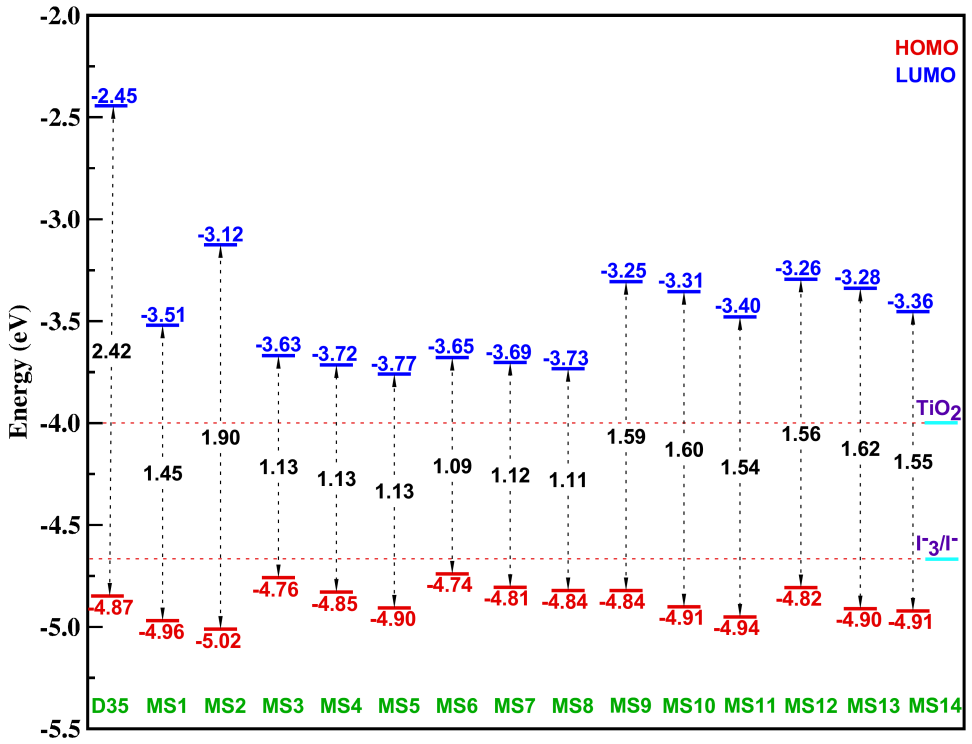

Fig. 5 Frontier molecular orbital (FMO) energies and energy gaps calculated at (U)B3LYP/6-31G(*d*, *p*) level of theory and basis set of the parent and designed dyes, compared with TiO_2 conduction band and I_3^{-1}/I^{-1} oxidation potential.

Table 4 The computed ionization potential (IP), electron affinity (EA), chemical hardness (h), hole (λ_h), electron (λ_e), and total (λ^{tot}) reorganization energies of the parent and designed dyes. IP, EA, and h values are obtained with (U)B3LYP/6-31+G(*d*, *p*) level of theory and basis set on the ground-state geometries. Energy values are reported in eV.

Dye	IP	EA	h	λ_h	λ_e	λ^{tot}
D35	6.09	1.54	2.27	0.239	0.519	0.758
MS1	6.09	2.69	1.70	0.206	0.400	0.607
MS2	6.21	2.25	1.98	0.337	0.501	0.838
MS3	5.80	2.96	1.42	0.156	0.259	0.415
MS4	5.89	3.04	1.43	0.146	0.261	0.407
MS5	5.94	3.09	1.43	0.146	0.264	0.409
MS6	5.72	3.03	1.35	0.164	0.226	0.390
MS7	5.79	3.07	1.36	0.152	0.227	0.380
MS8	5.82	3.10	1.36	0.147	0.232	0.379
MS9	5.96	2.50	1.73	0.193	0.338	0.531
MS10	6.04	2.57	1.73	0.230	0.345	0.575
MS11	6.07	2.66	1.70	0.241	0.336	0.577
MS12	5.90	2.58	1.66	0.173	0.298	0.470
MS13	5.98	2.60	1.69	0.186	0.306	0.492
MS14	6.00	2.68	1.66	0.192	0.311	0.503

to the change in the molecular geometry during the electron-transfer, it has more impact on the charge-transport than the outer (intermolecular) reorganization energy, whereas, the latter accounts for the effect of the surrounding medium.[76] The intramolecular reorganization energies are calculated according the the following equations[15]:

$$\lambda_h = (E_0^+ - E_+) + (E_+^0 - E_0) \quad (9)$$

$$\lambda_e = (E_0^- - E_-) + (E_-^0 - E_0) \quad (10)$$

$$\lambda^{tot} = \lambda_h + \lambda_e \quad (11)$$

where, λ_h, λ_e, and λ^{tot} are the hole, electron, and total reorganization energies, respectively, E_0 is the neutral ground-state energy, E_0^+ and E_0^- are the positively and negatively charged state energies calculated on the neutral ground-state geometry, E_+ and E_- are the energies of the optimized cationic and anionic states, E_+^0 and E_-^0 are energies of the neutral state calculated on the positively and negatively charged geometries, respectively.

The calculated reorganization energies are provided in Table 4. The open-shell dyes have low λ_h energies, much smaller than the closed-shell and the parent dye. The largest λ_h is observed for MS2 dye (0.337 eV), which is due to the large bending along the MS2 dye (Fig. S1). Also, the λ_e is smaller in the open-shell dyes as well, largest value is obtained for the parent dye (0.519

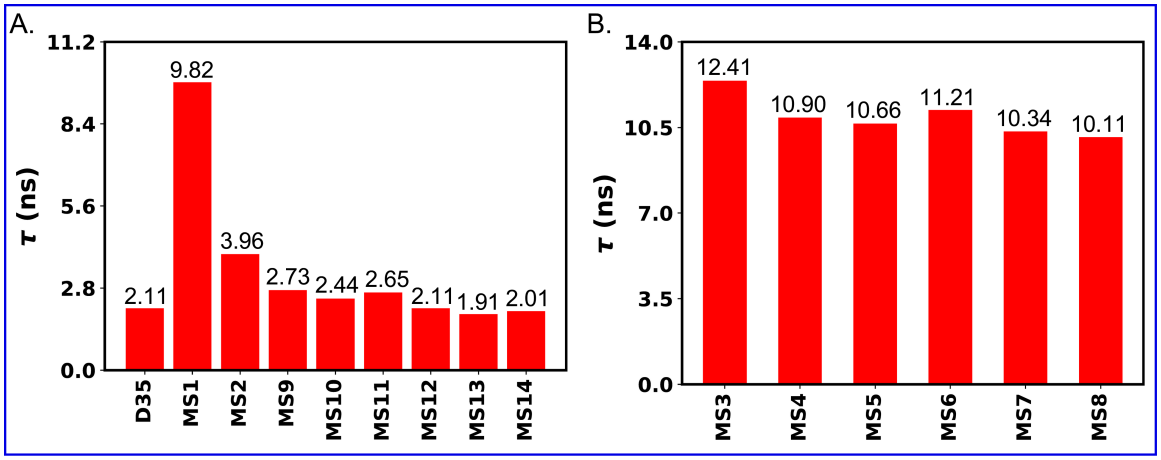

Fig. 6 Excited state lifetimes (τ) of the parent and designed dyes in their (A) closed-shell and (B) open-shell configurations, calculated at (U)B3LYP/6-31G(d, p) level of theory and basis set.

eV). A more planar geometry, delocalized orbital topology, and an increased π-conjugation reduces the reorganization energies of the open-shell dyes. The λ_h of all the dyes are smaller than the λ_e, which indicates the designed dye have a higher hole-transport ability.[15,77] Also, the calculated total reorganization energy (λ^{tot}) is smaller in the open-shell dyes than the closed-shell dyes, which indicates the open-shell dyes have increased ambipolar charge-transport character than the closed-shell dyes.[26,46] The smallest λ^{tot} (0.379 eV) is obtained for MS8 dye, which indicates this dye have increased charge-transfer ability than the other designed dyes. As the diradical character is increased in the open-shell dyes, the λ^{tot} is observed to decrease (Fig. 2D), larger dyes (MS6–MS8) with improved planarity reduce the total reorganization energy than the smaller dye (MS3–MS5).

3.7 Excited-state lifetime (τ)

Dyes with higher singlet excited-state lifetimes (τ) reduce the charge recombination process and increase the PCE of DSC.[78] The excited-state lifetimes of the designed dyes are calculated with the following equation[15,37] and compared with the parent dye, D35.

$$\tau = \frac{1.499}{E^2 \times f} \tag{12}$$

where, E is the energy (cm^{-1}), and f is the oscillator strength of the different transitions. The calculated τ values corresponding to the highest absorption peaks are provided in Fig. 6. Although, the calculated τ values for D35 dye is comparable with the other closed-shell dyes (2.00–4.00 ns), the open-shell dyes have significantly higher τ values (10.00–12.40 ns) than the closed-shell dyes, largest value is obtained for MS3 dye. This increase in the τ values indicates the charge-transfer efficiency is higher in the open-shell dyes than the closed-shell dyes.[15,37] Also, based on the calculated τ values, the open-shell dyes have more stability in the catatonic state than the closed-shell dyes.[37] Interestingly, due to the large quinoidal character, a significant increase in the τ value is observed for MS1 dye. Moreover, as the size of the designed dyes are increased, a reduction in the τ value is observed for both open-shell and closed-shell dyes.

The observed diradical character nicely correlates with the excited-state lifetimes of the open-shell dyes (Fig. 2F). In case of the open-shell dyes in a same series (MS3–MS5 and MS6–MS8), the dye with small diradical character found to have reduced excited-state lifetimes. The diradical character of MS3 dye (y = 0.096) is larger than the MS4 (y = 0.086) and MS5 (y = 0.065) dyes (see Table 1), therefore, the τ values found to decrease from MS3 to MS4 to MS5. Similar trend is observed in MS6–MS8 dyes as well, where dyes with smaller diradical character observed to have smaller excited-state lifetimes. This correlation between the diradical character and excited-state lifetimes indicates a small diradical character ($y < 0.10$) is beneficial in achieving higher excited-state lifetimes in the DSC dyes.

3.8 Intramolecular charge transfer (ICT) characteristics

A strong push-pull interactions in the D$-\pi-$A configurations induce efficient charge separations, facilitating intense ICT character. The charge-transfer properties of the parent and designed dyes are provided in Table 5. The spatial extent between the density depleted and incremented region is defined with the qualitative index, D_{CT}.[79] The observed D_{CT} is higher in the closed-shell dyes, which indicates the closed-shell dyes have prominent ICT character than the open-shell dyes. The order of the D_{CT} is observed as closed-shell > quinoidal > open-shell dyes. The highly aromatic thiadiazole units (Fig. S4–S5) of the BBT π-spacer probably acting as the charge trapping site, reducing the D_{CT} of the quinoidal and open-shell dyes.[71] As the size of the designed dyes are increased in the same series, the open-shell dyes have increased D_{CT}, whereas, the closed-shell dyes observed to have a reduced D_{CT} than the smaller dyes. It is interesting to note that a large overlap between the density depletion and increment centroids is oberved in the open-shell dyes ($H \geq D_{CT}$),[79] which is probably due to the delocalized spin distributions in the whole backbone of the dyes.

The total amount of the charge transferred due to the excitation is quantified with Δq. Due to a complete delocalized MOs (Fig. S8) and highly planar geometry (Fig. S2), the open-shell dyes

Table 5 The electronic properties of the parent and designed dyes calculated at (U)B3LYP/6-31G(*d, p*) level of theory and basis set. Charge-transfer distance (D_{CT}), total amount of charge transferred due to excitation (Δq), average of the two centroid along the charge transfer direction (H), excitation energy corresponding to the maximum absorbtion (E^*), exciton binding energy (E_b), open circuit voltage (V_{oc}), charge injection efficiency (ΔG_{inject}), and dye regeneration efficiency (ΔG_{reg}). All energy values are provided in eV, dipole moments in Debye, and distances are in Å.

Dye	D_{CT}	Δq	H	LHE	$\Delta\mu$	E^*	E_b	V_{oc}	ΔG_{inject}	ΔG_{reg}
D35	5.19	0.771	4.40	0.973	19.24	2.64	0.22	1.55	-1.77	0.17
MS1	4.17	0.642	3.85	0.916	12.87	1.48	0.03	0.49	-0.52	0.26
MS2	5.39	0.943	4.23	0.911	24.39	2.35	0.45	0.88	-1.33	0.32
MS3	2.75	1.120	3.76	0.951	14.79	1.19	0.06	0.37	-0.43	0.06
MS4	2.21	1.078	3.37	0.951	11.42	1.27	0.14	0.28	-0.42	0.15
MS5	2.21	1.204	3.24	0.954	12.81	1.27	0.14	0.23	-0.37	0.20
MS6	2.94	0.924	4.02	0.968	13.05	1.17	0.08	0.35	-0.43	0.04
MS7	2.46	0.901	3.82	0.967	10.64	1.22	0.10	0.31	-0.41	0.11
MS8	2.72	0.931	3.89	0.970	12.17	1.22	0.11	0.27	-0.31	0.21
MS9	6.06	0.781	5.72	0.983	22.71	2.18	0.59	0.75	-1.34	0.14
MS10	6.04	0.775	5.86	0.987	22.49	2.24	0.64	0.69	-1.33	0.21
MS11	6.64	0.817	5.94	0.983	26.06	2.22	0.68	0.60	-1.28	0.24
MS12	5.75	0.727	6.40	0.995	20.07	2.16	0.60	0.74	-1.34	0.12
MS13	5.34	0.689	6.50	0.997	17.66	2.21	0.59	0.72	-1.31	0.20
MS14	6.00	0.724	6.68	0.996	20.85	2.19	0.64	0.64	-1.28	0.21

have increased Δq than the closed-shell dyes. As the size of the dyes are increased (MS6–MS8, and MS12–MS14), a reduction in the total amount of charge-transfer is observed. Moreover, the quinoidal dye, MS1 is observed to have lowest Δq than the other open-shell and closed-shell dyes.

An enhanced ICT process increases the dipole moment of the sensitizer in the excitation process.[80] The changes in the calculated dipole moments are provided in Table 5. The observed $\Delta\mu$ is increased in the closed-shell dyes, largest value is obtained for MS11 dye. A large change in the dipole moment can induce nonlinear optical (NLO) properties in the designed dyes.[45] Also, the LHE is higher in the closed-shell dyes than the open-shell dyes.

In an excited-state, the photon absorbed by the sensitizer generates excitons, a charge neutral electron-hole pair bounded with exciton binding energy (E_b). The generated excitons needs to be separated effectively, which is a critical step in the DSC device operation.[76] The calculated E_b is provided in Table 5 and the dyes can be arranged as closed-shell > open-shell > quinoidal. The quinoidal and open-shell dyes (MS1, MS3–MS8) display significantly reduced E_b than the closed-shell dyes, which indicates faster charge separation is observed in the open-shell and quinoidal dyes than the closed-shell dyes.[15] Also, increasing the diradical character reduces E_b (Fig. 2I), which is due to a reduced electron-electron coupling between the unpaired electrons.

3.9 Charge injection (ΔG_{inject}) and regeneration efficiency (ΔG_{reg}) of the parent and designed dyes

The charge injection (ΔG_{inject}) and dye regeneration efficiency (ΔG_{reg}) of the designed dyes are critical parameters affecting the PCE of the DSC device. Here, ΔG_{inject} is calculated using equation 4 and ΔG_{reg} is computed according to equation 6. The computed ΔG_{inject} and ΔG_{reg} values are provided in Table 5.

The calculated ΔG_{inject} are negative, which indicates all the dyes have sufficient potential for electron injection into TiO_2 conduction band.[37,81] Also, the calculated values are greater than 0.20 eV, which indicates the designed dyes can inject electron efficiently.[15,82]

All the designed dyes (MS1–MS14) have a reduced V_{oc} and ΔG_{inject} efficiency than the parent dye, D35 (Table 5). It is evident from Fig. 5 that the calculated HOMO energy levels of the parent and designed dyes are very similar. However, due to a reduction in the FMOs energy gaps, the excitation energy is significantly reduced in the open-shell dyes than the closed-shell dyes. Therefore, the closed-shell dyes have a higher ΔG_{inject} than the open-shell dyes. Also, the LUMO energy levels of the open-shell dyes are closer to the TiO_2 conduction band (Fig. 5); therefore, reducing the V_{oc} and ΔG_{inject} in the open-shell dyes. It is interesting to note that, the quinoidal dye (MS1) also show a reduced ΔG_{inject} efficiency than the closed-shell dye, slightly larger than the open-shell dyes. Therefore, the dyes are arranged in terms of ΔG_{inject} as closed-shell > quinoidal > open-shell dyes. Also, increasing the diradical character in the same series of dyes (MS3–MS5, and MS6–MS8) reduces the ΔG_{inject} of the open-shell dyes (Fig. 2G), which is due to a more deeper HOMO energy level of the dyes with lower diradical character (MS4–MS5, and MS7–MS8). However, N substitution on the closed-shell dyes have negligible effect on the calculated ΔG_{inject} than the open-shell dyes.

The dye regeneration efficiency ΔG_{reg} depends on the HOMO energy level of the dye, provided same redox-shuttle is used for the regeneration purpose. There is no clear distinction in calculated ΔG_{reg} values between the closed-shell and open-shell dyes. However, it is evident from Table 5 that the MS6 dye with largest diradical character (y = 0.130) has smallest ΔG_{reg} (0.04 eV) among the designed dyes. Also, dye MS3 (y = 0.096) has very small ΔG_{reg} value, due to an increased HOMO energy level compared to the other dyes. Decreasing the diradical character increases the ΔG_{reg} (Fig. 2H), which is achieved by N substitution on the dye backbone. Therefore, atomistic substitution technique facilitates tuning of the dye electronic properties, which in turn can modulate the PCE of the DSC device.

4 Conclusions

We report several open-shell DSC dyes that can absorb photons in the near IR region and display unique electronic, optical, and charge-transport properties. The electronic structure of the open-shell and the closed-shell dyes are carefully exam-

ine to correlate their optical properties. While the open-shell dyes have larger backbone planarity and a high degree of π-conjugation, the closed-shell dyes have a reduced planarity and weak π-conjugation along the molecular backbone. Due to a very strong AFM coupling between the paired electrons in the closed-shell dyes, a larger singlet–triplet energy gaps is observed in the closed-shell dyes than the open-shell dyes. A small HOMO–LUMO energy gap inherent to the open-shell dyes significantly red-shifted the absorption wavelength is in the NIR region compared to the closed-shell dyes. A delocalized spin distribution of the open-shell dyes indicate thermodynamic stability; therefore, making these dyes as a synthetic target for DSC device fabrication. Calculation of the diradical character (y) of the open-shell dyes indicate a large y value ($y > 0.10$) reduce the dye regeneration and electron injection efficiencies, limiting the diradical character to be $y < 0.10$ in order to meet dye design criteria. The excited-state lifetimes of the open-shell dyes is significantly enhanced than the closed-shell dyes, which can reduce the recombination reaction and increase the PCE of the DSC device. The open-shell dyes have lower ionization potential and increased electron affinity, which indicates the open-shell dyes can easily loose and accept electrons during photoexcitation and regeneration process, respectively. Also, open-shell dyes are more susceptible for ambipolar charge-transfer than the closed-shell dyes. However, the closed-shell dyes have improved ICT character and higher injection efficiencies than the open-shell dyes. Therefore, co-sensitization of the designed closed-shell and open-shell dyes could be a promising technique for improving the PCE of a DCS device.[7,10,12,23,36,38] Also, designing redox-shuttles that aligns with the energy levels of the open-shell dyes to provide sufficient energetics can also maximize the DSC performance.[4,70,83] Our recommended approach for generating synthesis targets is to first screen dyes based on the diradical index and then narrow down the selection using open circuit voltage and regeneration efficiency for a specific DSC application. On a smaller set of dyes that meet previous criteria, one can evaluate exciton binding energies and the life times to narrow the choice to most suitable subset of dyes for synthesis.

Conflicts of interest

There are no conflicts to declare.

Acknowledgements

This work is supported by the National Science Foundation (NSF) under grant no. OIA-1757220. The DFT calculations are performed at the high-performance computing center at Mississippi State University, the Extreme Science and Engineering Discovery Environment (XSEDE) supported by NSF grant number ACI-1548562, and Texas Advanced Computing Center (TACC) at The University of Texas at Austin (Stampede 2, allocation, TG-CHE140141).

Notes and references

1 B. O'regan and M. Grätzel, *nature*, 1991, **353**, 737.
2 M. Grätzel, *nature*, 2001, **414**, 338.
3 K. Sharma, V. Sharma and S. Sharma, *Nanoscale Res. Lett.*, 2018, **13**, 381.
4 P. Brogdon, H. Cheema and J. H. Delcamp, *ChemSusChem*, 2018, **11**, 86–103.
5 B. E. Hardin, H. J. Snaith and M. D. McGehee, *Nat. Photonics*, 2012, **6**, 162–169.
6 P. Li, Z. Wang, C. Song and H. Zhang, *J. Mater. Chem. C*, 2017, **5**, 11454–11465.
7 H. Song, Q. Liu and Y. Xie, *ChemComm.*, 2018, **54**, 1811–1824.
8 S. Mathew, A. Yella, P. Gao, R. Humphry-Baker, B. F. Curchod, N. Ashari-Astani, I. Tavernelli, U. Rothlisberger, M. K. Nazeeruddin and M. Grätzel, *Nat. Chem.*, 2014, **6**, 242–247.
9 K. Kakiage, Y. Aoyama, T. Yano, K. Oya, T. Kyomen and M. Hanaya, *ChemComm.*, 2015, **51**, 6315–6317.
10 K. Kakiage, Y. Aoyama, T. Yano, K. Oya, J.-i. Fujisawa and M. Hanaya, *ChemComm.*, 2015, **51**, 15894–15897.
11 L. Zhang, X. Yang, W. Wang, G. G. Gurzadyan, J. Li, X. Li, J. An, Z. Yu, H. Wang and B. Cai, *ACS Energy Lett.*, 2019, **4**, 943–951.
12 J.-M. Ji, H. Zhou, Y. K. Eom, C. H. Kim and H. K. Kim, *Adv. Energy Mater.*, 2020, **10**, 2000124.
13 Y. Ni and J. Wu, *Tetrahedron Lett.*, 2016, **57**, 5426–5434.
14 M. K. Nazeeruddin, F. De Angelis, S. Fantacci, A. Selloni, G. Viscardi, P. Liska, S. Ito, B. Takeru and M. Grätzel, *J. Am. Chem. Soc.*, 2005, **127**, 16835–16847.
15 Y. Li, C. Sun, P. Song, F. Ma, N. Kungwan and M. Sun, *Sci. Rep.*, 2018, **8**, 1–18.
16 D. P. Hagberg, T. Marinado, K. M. Karlsson, K. Nonomura, P. Qin, G. Boschloo, T. Brinck, A. Hagfeldt and L. Sun, *J. Org. Chem.*, 2007, **72**, 9550–9556.
17 K. Hara, T. Sato, R. Katoh, A. Furube, Y. Ohga, A. Shinpo, S. Suga, K. Sayama, H. Sugihara and H. Arakawa, *J. Phys. Chem. B.*, 2003, **107**, 597–606.
18 Y. K. Eom, S. H. Kang, I. T. Choi, E. Kim, J. Kim, M. J. Ju and H. K. Kim, *RSC Adv.*, 2015, **5**, 80859–80870.
19 X. Wang, J. Yang, H. Yu, F. Li, L. Fan, W. Sun, Y. Liu, Z. Y. Koh, J. Pan and W.-L. Yim, *ChemComm.*, 2014, **50**, 3965–3968.
20 V. Sharma, D. Sahoo, N. Varghese, K. Mohanta and A. L. Koner, *RSC Adv.*, 2019, **9**, 30448–30452.
21 Y. Zhang, H. Cheema, A. E. London, A. Morales, J. D. Azoulay and J. H. Delcamp, *Phys. Chem. Chem. Phys.*, 2018, **20**, 2438–2443.
22 H. Cheema, A. Baumann, E. K. Loya, P. Brogdon, L. E. McNamara, C. A. Carpenter, N. I. Hammer, S. Mathew, C. Risko and J. H. Delcamp, *ACS Appl. Mater. Interfaces*, 2019, **11**, 16474–16489.
23 H. Cheema, J. Watson, A. Peddapuram and J. H. Delcamp, *ChemComm.*, 2020, **56**, 1741–1744.
24 S. Feng, Q.-S. Li, T. A. Niehaus and Z.-S. Li, *Org. Electron.*, 2017, **42**, 234–243.
25 M.-W. Lee, J.-Y. Kim, H.-G. Lee, H. G. Cha, D.-H. Lee and M. J. Ko, *J. Energy Chem.*, 2020, **54**, 208–216.
26 X. Hu, W. Wang, D. Wang and Y. Zheng, *J. Mater. Chem. C*, 2018, **6**, 11232–11242.

27 M. Nakano, R. Kishi, T. Nitta, T. Kubo, K. Nakasuji, K. Kamada, K. Ohta, B. Champagne, E. Botek and K. Yamaguchi, *J. Phys. Chem. A.*, 2005, **109**, 885–891.

28 K. Wang, L. Huang, N. Eedugurala, S. Zhang, M. A. Sabuj, N. Rai, X. Gu, J. D. Azoulay and T. N. Ng, *Adv. Energy Mater.*, 2019, **9**, 1902806.

29 M. Abe, *Chem. Rev.*, 2013, **113**, 7011–7088.

30 A. E. London, H. Chen, M. Sabuj, J. Tropp, M. Saghayezhian, N. Eedugurala, B. Zhang, Y. Liu, X. Gu, B. Wong, N. Rai and J. Azoulay, *Sci. Adv.*, 2019, **5**, eaav2336.

31 Y. Ni, S. Lee, M. Son, N. Aratani, M. Ishida, A. Samanta, H. Yamada, Y.-T. Chang, H. Furuta, D. Kim *et al.*, *Angew. Chem. Int. Ed.*, 2016, **55**, 2815–2819.

32 G. E. Rudebusch, J. L. Zafra, K. Jorner, K. Fukuda, J. L. Marshall, I. Arrechea-Marcos, G. L. Espejo, R. P. Ortiz, C. J. Gómez-García and L. N. Zakharov, *Nat. Chem.*, 2016, **8**, 753–759.

33 Z. Sun, Q. Ye, C. Chi and J. Wu, *Chem. Soc. Rev.*, 2012, **41**, 7857–7889.

34 D. P. Hagberg, X. Jiang, E. Gabrielsson, M. Linder, T. Marinado, T. Brinck, A. Hagfeldt and L. Sun, *J. Mater. Chem.*, 2009, **19**, 7232–7238.

35 A. Baumann, H. Cheema, M. A. Sabuj, L. E. McNamara, Y. Zhang, A. Peddapuram, S. T. Nguyen, D. L. Watkins, N. I. Hammer and N. Rai, *Phys. Chem. Chem. Phys.*, 2018, **20**, 17859–17870.

36 C.-P. Lee, R. Y.-Y. Lin, L.-Y. Lin, C.-T. Li, T.-C. Chu, S.-S. Sun, J. T. Lin and K.-C. Ho, *RSC Adv.*, 2015, **5**, 23810–23825.

37 M. Li, L. Kou, L. Diao, Q. Zhang, Z. Li, Q. Wu, W. Lu, D. Pan and Z. Wei, *J. Phys. Chem. C.*, 2015, **119**, 9782–9790.

38 Y. Hao, Y. Saygili, J. Cong, A. Eriksson, W. Yang, J. Zhang, E. Polanski, K. Nonomura, S. M. Zakeeruddin and M. GraÌĺtzel, *ACS Appl. Mater. Interfaces*, 2016, **8**, 32797–32804.

39 J. Zhang, H.-B. Li, S.-L. Sun, Y. Geng, Y. Wu and Z.-M. Su, *Journal of Materials Chemistry*, 2012, **22**, 568–576.

40 L. Bianchi, X. Zhang, Z. Chen, P. Chen, X. Zhou, Y. Tang, B. Liu, X. Guo and A. Facchetti, *Chem. Mater.*, 2019, **31**, 6519–6529.

41 Y. Liu, H. Phan, T. S. Herng, T. Y. Gopalakrishna, J. Ding and J. Wu, *Chem. Asian J.*, 2017, **12**, 2177–2182.

42 N. N. Ghosh, A. Chakraborty, S. Pal, A. Pramanik and P. Sarkar, *Phys. Chem. Chem. Phys.*, 2014, **16**, 25280–25287.

43 N. N. Ghosh, S. Saha, A. Pramanik, P. Sarkar and S. Pal, *Comput. Theor. Chem.*, 2020, **1182**, 112846.

44 K. Hara, M. Kurashige, Y. Dan-oh, C. Kasada, A. Shinpo, S. Suga, K. Sayama and H. Arakawa, *New J. Chem.*, 2003, **27**, 783–785.

45 G.-J. Zhao, R.-K. Chen, M.-T. Sun, J.-Y. Liu, G.-Y. Li, Y.-L. Gao, K.-L. Han, X.-C. Yang and L. Sun, *Chem.: Eur. J.*, 2008, **14**, 6935–6947.

46 Z. Lin, L. Chen, Q. Xu, G. Shao, Z. Zeng, D. Wu and J. Xia, *Org. Lett.*, 2020, **22**, 2553–2558.

47 M. A. Sabuj, M. M. Huda and N. Rai, *Designing Donor-Acceptor Conjugated Macrocycles with Polyradical Character and Global (Anti) Aromaticity*, `http://dx.doi.org/10.2139/ssrn.3589834/`.

48 A. Saha and B. Ganguly, *RSC Adv.*, 2020, **10**, 15307–15319.

49 R. A. Vogt, T. G. Gray and C. E. Crespo-Hernandez, *J. Am. Chem. Soc.*, 2012, **134**, 14808–14817.

50 M. J. Frisch, G. W. Trucks, H. B. Schlegel, G. E. Scuseria, M. A. Robb, J. R. Cheeseman, G. Scalmani, V. Barone, G. A. Petersson, H. Nakatsuji, X. Li, M. Caricato, A. V. Marenich, J. Bloino, B. G. Janesko, R. Gomperts, B. Mennucci, H. P. Hratchian, J. V. Ortiz, A. F. Izmaylov, J. L. Sonnenberg, D. Williams-Young, F. Ding, F. Lipparini, F. Egidi, J. Goings, B. Peng, A. Petrone, T. Henderson, D. Ranasinghe, V. G. Zakrzewski, J. Gao, N. Rega, G. Zheng, W. Liang, M. Hada, M. Ehara, K. Toyota, R. Fukuda, J. Hasegawa, M. Ishida, T. Nakajima, Y. Honda, O. Kitao, H. Nakai, T. Vreven, K. Throssell, J. A. Montgomery, Jr., J. E. Peralta, F. Ogliaro, M. J. Bearpark, J. J. Heyd, E. N. Brothers, K. N. Kudin, V. N. Staroverov, T. A. Keith, R. Kobayashi, J. Normand, K. Raghavachari, A. P. Rendell, J. C. Burant, S. S. Iyengar, J. Tomasi, M. Cossi, J. M. Millam, M. Klene, C. Adamo, R. Cammi, J. W. Ochterski, R. L. Martin, K. Morokuma, O. Farkas, J. B. Foresman and D. J. Fox, *GaussianËIJ16, B.01*, 2016, Gaussian Inc. Wallingford CT.

51 A. D. Becke, *J. Chem. Phys.*, 1993, **98**, 1372–1377.

52 P. Stephens, F. Devlin, C. Chabalowski and M. J. Frisch, *J. Phys. Chem.*, 1994, **98**, 11623–11627.

53 M. M. Francl, W. J. Pietro, W. J. Hehre, J. S. Binkley, M. S. Gordon, D. J. DeFrees and J. A. Pople, *J. Chem. Phys.*, 1982, **77**, 3654–3665.

54 L. Noodleman, *J. Chem. Phys.*, 1981, **74**, 5737–5743.

55 S. Canola, J. Casado and F. Negri, *Phys. Chem. Chem. Phys.*, 2018, **20**, 24227–24238.

56 P. v. R. Schleyer, M. Manoharan, Z.-X. Wang, B. Kiran, H. Jiao, R. Puchta and N. J. van Eikema Hommes, *Org. Lett.*, 2001, **3**, 2465–2468.

57 K. Wolinski, J. F. Hinton and P. Pulay, *J. Am. Chem. Soc.*, 1990, **112**, 8251–8260.

58 J. R. Cheeseman, G. W. Trucks, T. A. Keith and M. J. Frisch, *J. Chem. Phys.*, 1996, **104**, 5497–5509.

59 R. Bauernschmitt and R. Ahlrichs, *Chem. Phys. Lett.*, 1996, **256**, 454–464.

60 A. Austin, G. A. Petersson, M. J. Frisch, F. J. Dobek, G. Scalmani and K. Throssell, *J. Chem. Theory Comput.*, 2012, **8**, 4989–5007.

61 C. Adamo and V. Barone, *J. Chem. Phys.*, 1999, **110**, 6158–6170.

62 Y. Zhao and D. G. Truhlar, *Theoretical Chemistry Accounts*, 2008, **120**, 215–241.

63 T. Yanai, D. P. Tew and N. C. Handy, *Chem. Phys. Lett.*, 2004, **393**, 51–57.

64 J.-D. Chai and M. Head-Gordon, *Phys. Chem. Chem. Phys.*, 2008, **10**, 6615–6620.

65 S. Miertuš, E. Scrocco and J. Tomasi, *Chemical Physics*, 1981, **55**, 117–129.

66 M. Cossi, V. Barone, R. Cammi and J. Tomasi, *Chem. Phys. Lett.*, 1996, **255**, 327–335.
67 X. Song, X. Yang, H. Wang, J. An, Z. Yu, X. Wang, A. Hagfeldt and L. Sun, *Sol. Energy*, 2019, **187**, 274–280.
68 M. Nakano and B. Champagne, *J. Chem. Phys.*, 2013, **138**, 244306.
69 M. Nakano and B. Champagne, *j. Phys. Chem. Lett.*, 2015, **6**, 3236–3256.
70 S. M. Feldt, E. A. Gibson, E. Gabrielsson, L. Sun, G. Boschloo and A. Hagfeldt, *J. Am. Chem. Soc.*, 2010, **132**, 16714–16724.
71 G. Xue, X. Hu, H. Chen, L. Ge, W. Wang, J. Xiong, F. Miao and Y. Zheng, *ChemComm.*, 2020, **56**, 5143–5146.
72 D. P. Hagberg, T. Edvinsson, T. Marinado, G. Boschloo, A. Hagfeldt and L. Sun, *ChemComm.*, 2006, 2245–2247.
73 L. L. Estrella, M. P. Balanay and D. H. Kim, *J. Phys. Chem. A.*, 2018, **122**, 6328–6342.
74 R. Soto-Rojo, J. Baldenebro-López and D. Glossman-Mitnik, *Phys. Chem. Chem. Phys.*, 2015, **17**, 14122–14129.
75 R. A. Marcus, *Rev. Mod. Phys.*, 1993, **65**, 599.
76 J.-L. Brédas, D. Beljonne, V. Coropceanu and J. Cornil, *Chem. Rev.*, 2004, **104**, 4971–5004.
77 L. Deng, W. Shen, X. Xie, L. Jiang, B. Liu and M. Li, *Struct. Chem.*, 2012, **23**, 97–106.
78 K. Chaitanya, X.-H. Ju and B. M. Heron, *RSC Adv.*, 2014, **4**, 26621–26634.
79 T. Le Bahers, C. Adamo and I. Ciofini, *J. Chem. Theory Comput.*, 2011, **7**, 2498–2506.
80 R. Misra and S. P. Bhattacharyya, *Intramolecular Charge Transfer: Theory and Applications*, John Wiley & Sons, 2018.
81 U. Mehmood, I. A. Hussein, M. Daud, S. Ahmed and K. Harrabi, *Dyes Pigm.*, 2015, **118**, 152–158.
82 R. Katoh and A. Furube, *J. Photochem. Photobiol. C*, 2014, **20**, 1–16.
83 R. R. Rodrigues, J. M. Lee, N. S. Taylor, H. Cheema, L. Chen, R. C. Fortenberry, J. H. Delcamp and J. W. Jurss, *Dalton Trans.*, 2020, **49**, 343–355.